



# Reducing the thermal hazard of hydrophobic silica aerogels by using dimethyldichlorosilane as modifier

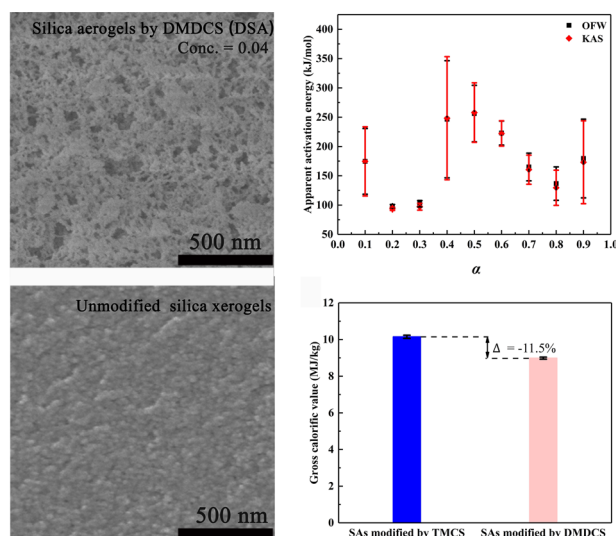
Yinfeng Wang<sup>1</sup> · Zhi Li<sup>1,2</sup> · Lukas Huber<sup>2</sup> · Xiaoxu Wu<sup>1,3</sup> · Siqi Huang<sup>1</sup> · Yan Zhang<sup>1</sup> · Rui Huang<sup>1</sup> · Qiong Liu<sup>1</sup>

Received: 7 June 2019 / Accepted: 18 October 2019 / Published online: 8 November 2019  
© Springer Science+Business Media, LLC, part of Springer Nature 2019

## Abstract

Reducing organic groups on hydrophobic silica aerogels (SA) is worth exploring for lowering their thermal hazard risk. In this work, we used dimethyldichlorosilane (DMDCS) to modify silica aerogels, investigated the effects of DMDCS concentration and focused on the thermal hazard assessment of the DMDCS modified SA (DSA). It was turned out that the DSA had less  $-\text{CH}_3$  content in spite of the thermal stability close to the trimethylchlorosilane modified SA (TSA), about 240 °C. The kinetics study suggested the apparent activation energy ( $E_a$ ) could be divided into two segments, corresponding to the two processes in the pyrolysis. The positive enthalpy and entropy changes indicated that the thermal oxidation of the DSA was an exothermic reaction, which could not occur without external energy supply. The average  $E_a$  of the DSA was far larger than that of the TSA and the gross calorific value of the DSA decreased by about 12% compared with that of the TSA. All these results drew a conclusion that the DMDCS modified SA reduced the thermal hazard to some degree, which provided one possible solution to further lower the thermal hazard of hydrophobic SA.

## Graphical Abstract



✉ Zhi Li  
lzwx1989@gmail.com

<sup>1</sup> School of Resources and Safety Engineering, Central South University, 410083 Changsha, PR China

<sup>2</sup> Laboratory for Building Energy Materials and Components, Swiss Federal Laboratories for Materials Science and Technology, Empa, Überlandstrasse 129, 8600 Dübendorf, Switzerland

<sup>3</sup> School of Economics and Management, Changsha University, 410003 Changsha, PR China

## Highlights

- Dimethyldichlorosilane modified silica aerogels (DSA) were prepared at the optimum concentration of 4%.
- Kinetic and thermodynamic behavior of DSA were studied in detail.
- DSA has larger apparent activation energy than trimethylchlorosilane modified silica aerogels (TSA).
- DSA has lower thermal hazard than TSA for a less gross calorific value.

**Keywords** Hydrophobic silica aerogels · Thermal hazard · Dimethyldichlorosilane · Kinetics · Thermodynamic parameter

## 1 Introduction

Silica aerogels (SA) have been widely used in various fields, which are a type of mesoporous materials with some excellent physicochemical properties, for instance, a low density of 0.003–0.500 g/cm<sup>3</sup>, a high porosity of over 90%, a large specific surface area of 500–1200 m<sup>2</sup>/g, and a low thermal conductivity of 0.01–0.03 W/(m·K) [1, 2]. SA have been proved to be promising materials in various applications like aerospace [3], adsorption [4], catalyst supports [5], and drug delivery and targeting systems [6]. But most importantly, SA can obtain wide usages in the field of thermal insulation because of their excellent thermal insulation performance [7, 8].

For a long time, the primary preparation technology of aerogels is to dry wet gels under supercritical condition [1], e.g., supercritical extraction of ethanol in liquid CO<sub>2</sub>. However, the high equipment costs, safety problems, and the deficiency of continuously industrial production of supercritical drying limit the wide application of SA. Developing the application of advanced equipment and new green materials is a strong measure to control the hazard [9]. Under the efforts of the scientific community and industry, the preparation technology of aerogels under ambient pressure drying (APD) is gradually becoming popular. The core step for synthesizing ambient pressure dried aerogels is the surface modification, which introduces a certain number of organic functional groups (e.g., alkyl) onto the skeletons of gels [10], leading to a reduction of the capillary pressure. This vital procedure is necessary to avoid the destruction of the three-dimensional network structure of SA during APD. On the other hand, the introduced organic functional groups are flammable [11, 12], which is an unavoidable problem we must consider. For thermal insulation materials, the usage environment is so complicated that insulation materials have to face a high temperature and even external heat flux produced by some readily flammable materials.

In reality, people habitually tend to consider aerogel materials as incombustible materials due to their excellent properties, especially their thermal insulation performance. There is little attention drawn on the fire safety of aerogel materials, which definitely increases the thermal hazard risk of aerogels. As the usage of aerogel materials expands

increasingly, this risk is getting worse. In our previous work, we investigated and compared the fire performance of supercritically dried SA and ambient pressure dried SA and demonstrated the flammability of hydrophobic SA [11]. In recent years, Ghazi Wakili et al. reported their research on the reaction of ceramic fiber/aerogels to fire exposure [13]; He and Huang et al. also studied the effects of heat treatment on hydrophobic SA and clarified the variations of O/Si, C/Si values, and the products during pyrolysis process [14]. These researches further verified the thermal hazard risks of hydrophobic SA. At present, it is the exact time for us to take the flammability and thermal degradation of hydrophobic SA into consideration. Hence, the remained problem is for us to find out how to reduce these risks.

Just as mentioned above, it is the organic groups introduced by surface modification that bring the thermal hazards to hydrophobic SA. This conclusion can be strongly supported by many thermal analyses [14–17], which reveals that the exothermic reactions during the pyrolysis process should be ascribed to the thermal oxidation of organic groups (e.g., –CH<sub>3</sub>). Obviously, the higher the content of organic groups, the higher the thermal hazard risk of hydrophobic SA. Hence, reducing the content of organic groups without compromising other properties or choosing a more appropriate type of organic functional groups are our directions to solve these problems.

Currently, trimethylsilyl (TMS) has been common functional groups for surface modification of aerogels [18, 19], such as trimethylchlorosilane (TMCS), hexamethyldisiloxane (HMDSO) [20], hexamethyldisilazane (HMDZ), etc. Each TMS is composed of three –CH<sub>3</sub> groups. Assuming that for a stable hydrophobicity, the quantity of functional groups on the skeletons of gels is approximately constant, decreasing the number of methyl in the functional groups is of great importance to reduce the thermal hazard risk. As it is known, dimethylsilyl (DMS) has less –CH<sub>3</sub> groups to graft onto gels during surface modification compared with TMS. Therefore, the challenge we are facing is whether it is feasible to lower the flammability of hydrophobic SA by replacing TMS groups with DMS groups.

In this study, we primarily focused on investigating the thermal hazard of hydrophobic SA modified with DMS

groups. Hence, we first prepared the DMS modified hydrophobic SA and compared them with the classical hydrophobic SA modified by TMS groups on the aspect of basic physicochemical properties. Followed by the thermal analyses, kinetic and thermodynamic analyses were carried out to evaluate their thermal hazard. The research outcome demonstrated that this strategy is beneficial to lower the thermal hazard of hydrophobic SA, which can provide a technical guide on further reducing the flammability of SA.

## 2 Experimental methodology

### 2.1 Raw materials and preparation

Tetraethylorthosilicate (TEOS, 98%), dimethyldichlorosilane (DMDCS, 98%), from Aladdin, China, were used as the precursor and surface modifier. Other chemicals including ethanol (EtOH), TMCS, n-hexane, hydrochloric acid (HCl), and ammonium hydroxide ( $\text{NH}_3\cdot\text{H}_2\text{O}$ ) were chemical pure grade, which were purchased from Sino-pharm Chemical Reagent Co., Ltd. (SCRC, China).

The acid-base catalyzed sol–gel process and derivatization modification method were used to prepare hydrophobic SA in this work. The optimum molar ratio of TEOS: EtOH:  $\text{H}_2\text{O}$ : HCl:  $\text{NH}_3\cdot\text{H}_2\text{O}$  was fixed at 1: 9.6: 2.2:  $1.6 \times 10^{-3}$ :  $9.7 \times 10^{-3}$  referring to our previous work [21]. The first step was to mix TEOS, EtOH, DI  $\text{H}_2\text{O}$ , and 0.1 M HCl together and stir for 10 min in a 100 mL beaker. After completing the hydrolysis in a 45 °C water bath for 9 h, 0.5 M  $\text{NH}_3\cdot\text{H}_2\text{O}$  was added in the mixed sol and stirred for 5 min. The gelation usually occurred within 30 min after the alcogels were made airtight for 4 h for strengthening the gel network. After aging, the alcogels were placed in n-hexane at 45 °C for solvent exchange. The alcogels were cut into small pieces and were immersed in a mixture of DMDCS/n-hexane solvent to perform the surface modification, during which the percentage of DMDCS in the solvent was elevated from 2 to 10%. Finally, the wet alcogels were washed in n-hexane for several times and dried at 120 °C for 4 h under ambient pressure to get hydrophobic SA in granular form. In this work, the as-prepared DMDCS modified SA (DSA) and TMCS modified SA were denoted as DSA and trimethylchlorosilane modified SA (TSA), respectively.

### 2.2 Methods of characterization

The bulk density ( $\rho_b$ ) of SA was measured by the Archimedes principle. Specifically, the SA was pressed

into deionized water to measure volume displacement by using an ultrafine steel wire. The porosity was determined by Eq. (1) [22]:

$$\text{Porosity} = \left(1 - \frac{\rho_b}{\rho_s}\right) \times 100\%, \quad (1)$$

where  $\rho_s$  is the skeletal density of SA, usually about 2200 kg/m<sup>3</sup> [15, 17, 23]. The pH was monitored by accurate pH test papers ranging between 0.5 and 5.0 (Newstar, China). The thermal conductivity instrument (TC3000E, XIATECH, China) based on transient hot-wire method was used to measure the thermal conductivity at 25 °C. First, the SA samples were ground into fine powders with 200 mesh sieve and then the kapton sensor was insert into SA powders through the slit on the stainless steel sample holder with 500 g weight on silica aerogel powders. For thermal conductivity measurement, each sample was tested over three times and the averages were taken as the final results. The microstructures were observed using a double beam microscope (Helios Nanolab G3UC, FEI). Furthermore, the hydrophobicity was characterized by a contact angle meter (JC2000D1, Shanghai Zhongchen Instrument) through putting a water droplet of 5  $\mu\text{L}$  on the sample surface and the contact angles were acquired by the image processing program, ImageJ [24].

The Quadrasorb SI-3MP analyzer (Quantachrome, USA) was used to test the  $\text{N}_2$  adsorption–desorption isotherms at 77 K with three specimens for each recipe. The specific surface area and pore size distribution (PSD) were calculated using the Brunauer–Emmett–Teller method [25] and Barrette–Joynere–Halenda method from the desorption branch [26], respectively. The chemical bonds were studied by Fourier transform infrared spectroscopy, which was tested by a Nicolet iS50 (Thermo Fisher Scientific, USA) by pressing silica aerogel pieces in a KBr pellet and collecting the spectra from 400 to 4000  $\text{cm}^{-1}$ .

Thermogravimetric analysis (TG, STA 449F3, NETZSCH) was carried out at three different heating rates, i.e., 10, 15, 25 °C/min, from room temperature to 1000 °C in air to investigate the thermal stability, kinetics, and thermodynamic analyses of SA [27–30]. The temperature resolution is 0.001 K and the balance resolution is 0.1  $\mu\text{g}$ . An oxygen bomb calorimeter (C3000, IKA, Germany) was used to measure the gross calorific value (GCV) following the ISO 1716: 2010 standard. It should be pointed out that the error bars used in this study are standard errors and over three specimens were tested for the calculation of the average values and standard errors.

### 2.3 Kinetics and thermodynamic analysis

The kinetic equation of chemical reaction can be written as Eq. (2).

$$\frac{d\alpha}{dt} = k(T)f(\alpha) \quad (2)$$

in which,  $\alpha$  is the conversion rate and can be calculated as

$$\alpha = \frac{m_i - m_\alpha}{m_i - m_\infty} \quad (3)$$

where  $m_i$ ,  $m_\alpha$ , and  $m_\infty$  are the initial mass, the mass at  $\alpha$ , and the finally residual mass, respectively.  $f(\alpha)$  is a reaction model [31], which reflects the reaction mechanism.  $k(T)$  is reaction rate constant and is usually defined as

$$k(T) = A \exp\left(-\frac{E_a}{RT}\right), \quad (4)$$

where  $A$  and  $E_a$  is a preexponential factor and apparent activation energy, respectively.  $R$  is the universal gas constant, 8.314 J/(K·mol). Therefore, the fundamental expression of the analytical method to calculate kinetic parameters can be described as follows.

$$\frac{d\alpha}{dt} = A \exp\left(-\frac{E}{RT}\right)f(\alpha) \quad (5)$$

Under nonisothermal conditions with a constant heating rate, the temperature can be expressed as,

$$T = T_0 + \beta t \quad (6)$$

where  $\beta$  is the heating rate and  $T_0$  is the initial temperature.

After combining Eq. (6), the conversion rate can be transformed into a temperature-derivative, i.e.,

$$\frac{d\alpha}{dT} = \frac{A}{\beta} \exp\left(-\frac{E_a}{RT}\right)f(\alpha) \quad (7)$$

Rearrange Eq. (7) to separate variables  $\alpha$  and  $T$ , and then integrate it.

$$G(\alpha) = \int_0^\alpha \frac{d\alpha}{f(\alpha)} = \frac{A}{\beta} \int_0^T \exp\left(-\frac{E_a}{RT}\right)dT \quad (8)$$

#### 2.3.1 Flynn–Wall–Ozawa (FWO) method

In the FWO method, after introducing Doyle's approximation, it can obtain the linear form [32, 33].

$$\ln \beta = \ln\left(\frac{AE}{RG(\alpha)}\right) - 5.3305 - 1.052 \frac{E}{RT} \quad (9)$$

For various heating rates at a fixed conversion rate  $\alpha$ , the  $\ln \beta$  and the corresponding  $1/T$  can be fitted to a straight line. Finally, the apparent  $E_a$  can be calculated from the slope,  $-1.052E/R$ .

#### 2.3.2 Kissinger–Akahira–Sunose (KAS) method

The following equation is employed in KAS method [34].

$$\ln\left(\frac{\beta}{T^2}\right) = \ln\left(\frac{AR}{EG(\alpha)}\right) - \frac{E}{RT} \quad (10)$$

At each degree of conversion  $\alpha$ , the  $\ln(\beta^2/T)$  and  $1/T$  data points obtained from different heating rates were fitted to a straight line. Then the  $E_a$  can be calculated by the slope,  $-E/R$ .

#### 2.3.3 Thermodynamic analysis

Based on obtained apparent activation energy, the thermodynamic parameters including the pre-exponential factor ( $A$ ), the change of enthalpy ( $\Delta H$ ), free Gibbs energy ( $\Delta G$ ), and entropy ( $\Delta S$ ) can be calculated as per the following equations [35]:

$$A = \beta E_a \exp\left(\frac{E_a}{RT_m}\right)/RT_m^2 \quad (11)$$

$$\Delta H = E_a - RT_\alpha \quad (12)$$

$$\Delta G = E_a + RT_m \ln\left(\frac{k_B T_m}{hA}\right) \quad (13)$$

$$\Delta S = \frac{\Delta H - \Delta G}{T_m} \quad (14)$$

where  $T_m$  and  $T_\alpha$  are the peak temperature on DTG and the temperature at a conversion of  $\alpha$ , respectively;  $k_B$  and  $h$  are Boltzmann constant ( $1.381 \times 10^{-23}$  J/K) and Plank constant ( $6.626 \times 10^{-34}$  J·s), respectively.

## 3 Results and discussion

### 3.1 Physicochemical properties

The pictures of the unmodified xerogels and the DSA with different DMDCS concentration are presented in Fig. 1, in which the DSA with the DMDCS concentration at 4–6% shows light blue, indicating a better surface modification. Figure 2 compares the density, porosity, and thermal conductivity of the prepared DSA modified with different concentration from 2 to 10%. It is obvious that the DSA at

**Fig. 1** Pictures of the unmodified xerogels and the DSA (0.5 g) with various DMDCS concentration between 2 and 10%

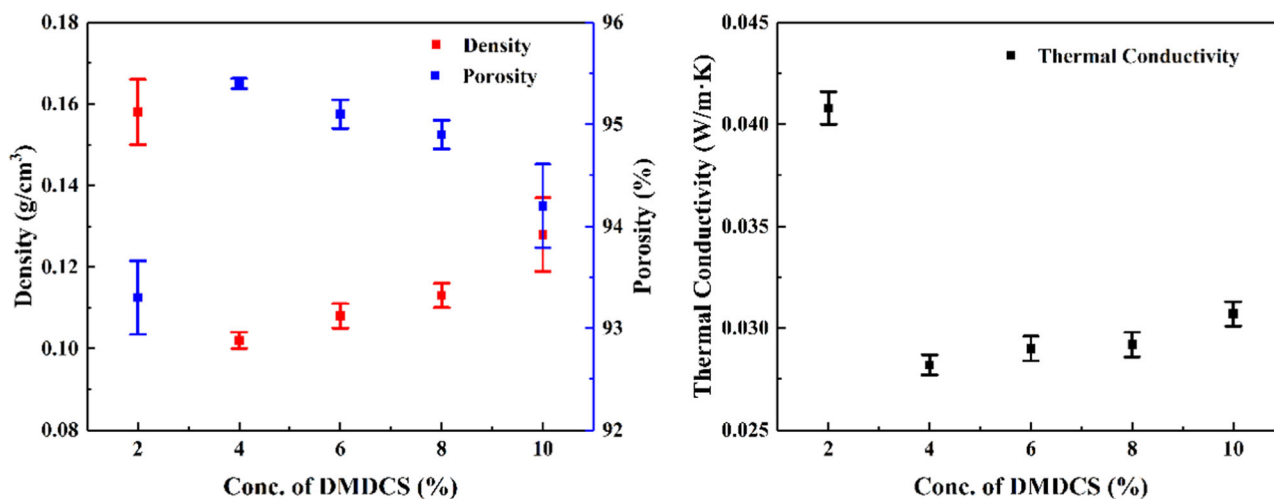
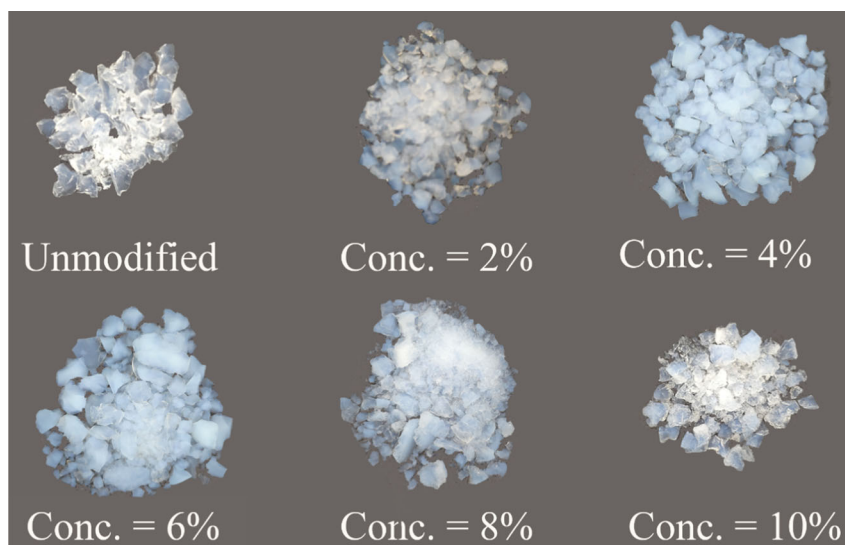


**Fig. 2** The changes of **a** density, porosity, and **b** thermal conductivity of DSA

the DMDCS concentration of 4% has the lowest density and thermal conductivity and the highest porosity. When the DMDCS concentration increases from 4 to 10%, the density and thermal conductivity increase slightly while the porosity decreases. The relatively larger thermal conductivity of the DSA should be caused by the compaction (500 g weight) during the measurement and unoptimized preparation parameters.

During the modification, the wet gels were immersed into *n*-hexane/DMDCS mixture solvent in a sealed breaker. With the surface modification proceeding, the derived by-product, i.e., HCl, was continuously generated in the mixture solvent, which resulted in an acid environment. As the DMDCS concentration increases, more HCl is generated and lead to a decreasing pH, as listed in Table 1. In an overly acid mixture solvent, the surface modification is hard

**Table 1** The pH of the different DMDCS concentration in the solvent

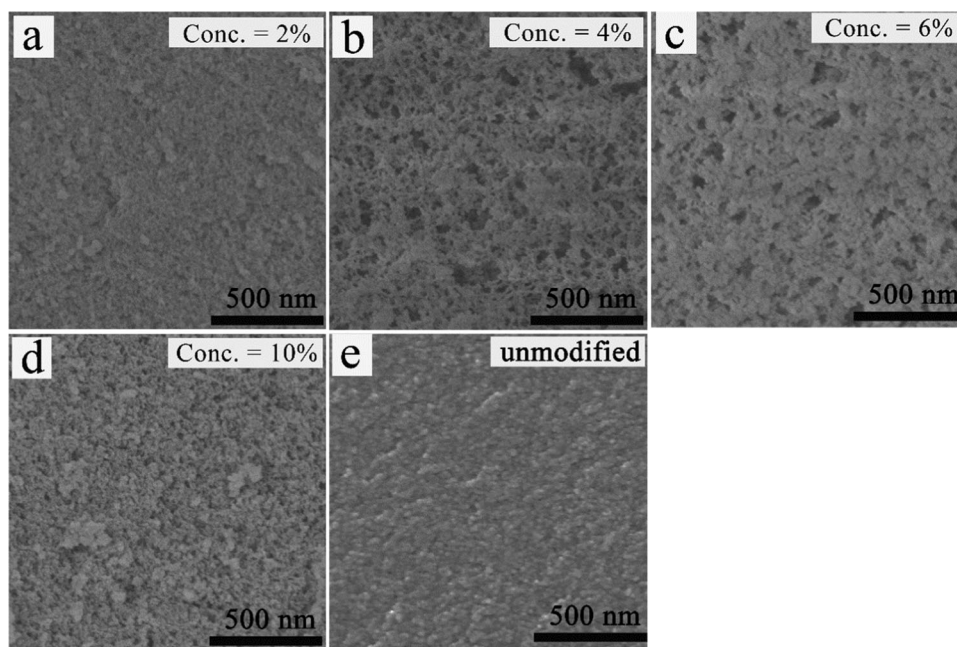
Concentration	2%	4%	6%	8%	10%
pH	2.5–3.0	2.0–2.5	1.5–2.0	1.0–1.5	1.0–1.5

to proceed because a large number of H<sup>+</sup> in the acidic solvent can hinder the reaction between DMDCS and the Si–OH groups on the wet gels due to chemical equilibrium. Besides, because of the two reactive sites, DMDCS may react with themselves, which results in a part of DMDCS losing the efficacy of surface modification. Thus, the appropriate concentration of DMDCS is vital for high-efficiency surface modification.

The typical microstructures of as-prepared DSA and the unmodified xerogels are presented in Fig. 3, which shows



**Fig. 3** Microstructures of DSA modified with various DMDCS concentration, **a** 2%, **b** 4%, **c** 6%, **d** 10%, and **e** unmodified xerogels



the influence of the modification treatment in different DMDCS concentrations on the DSA. In Fig. 3b it can be seen that the DSA modified in a DMDCS concentration being 4% displays a more porous structure compared with other DMDCS concentrations. When the DMDCS concentration is <4% or >6%, the pore size decreases significantly and a denser microstructure appears. This can be explained as follows: When the DMDCS concentration is <4% as presented in Fig. 3a, the number of Si-CH<sub>3</sub> groups is so less that the gel surface cannot acquire an adequate modification; while the DMDCS concentration is over 6% as shown in Fig. 3c, d, the overly acidic environment restrains the surface modification as mentioned above. Besides, DMDCS render themselves at high concentration and readily react with each other, which also impedes the surface modification. All of these cases result in the shrinkage or even destruction during APD. The variation of the microstructure of DSA exactly corresponds to the change of the density.

Figure 4a compares the N<sub>2</sub> adsorption–desorption isotherms of the DSA modified by different DMDCS concentrations and the PSD is presented in Fig. 4b. Obviously, all the samples exhibit typical type IV isotherms and the hysteresis loops of type H3, which indicate the attribution of mesoporous materials and the existence of slit-like pores [36]. The detailed pore parameters are listed in Table 2 with the typical specific surface area of more than 850 m<sup>2</sup>/g. Furthermore, corresponding to the microstructure, the average pore size of DSA modified at the DMDCS concentration of 4% is larger than the others.

In contrast to the FTIR spectra of the unmodified xerogels, which is shown from Fig. 5, the FTIR spectra of the

DSA modified by different DMDCS concentration are almost the same. The outstanding peak with the absorption spectra around 1090 cm<sup>-1</sup> is corresponding to the asymmetric flexible vibration mode of Si–O–Si bond [21], while the inconspicuous peaks at 800 and 460 cm<sup>-1</sup> belongs to the symmetric vibration and bending vibration of Si–O–Si bond. The absorption spectra around 2954 and 1398 cm<sup>-1</sup> just correspond to the C–H bond and the Si–C bond appears around 1265 and 845 cm<sup>-1</sup> [37]. The existence of these characteristic functional groups indicates a successful surface modification [38]. Compared with unmodified xerogels, the –OH intensities were significantly reduced, which also implies that the organic groups have been grafted on the skeleton of the DSA with the replacement of Si–OH groups. These introduced organic groups exactly constitute the chemical foundation of the hydrophobicity of the DSA.

Furthermore, the hydrophobicity of DSA has been confirmed by the water contact angle as shown in Fig. 6. Obviously, the maximum contact angle appears at 4% DMDCS concentration and the value is 154°. This result is consistent with our former analyses to some extent.

### 3.2 Thermostability analysis

As shown in Fig. 7a, b, the TG curves of DSA and TSA both have a slight weight before 150 °C, indicating the evaporation of water and residual organic solvents [17]. Furthermore, the sharp weight losses from 250 to 400 °C on the TG curves are accompanied by obvious exothermic peaks on the DSC curves. These processes are commonly attributed to the thermal oxidative decomposition of Si–CH<sub>3</sub> groups on the skeletons [12].

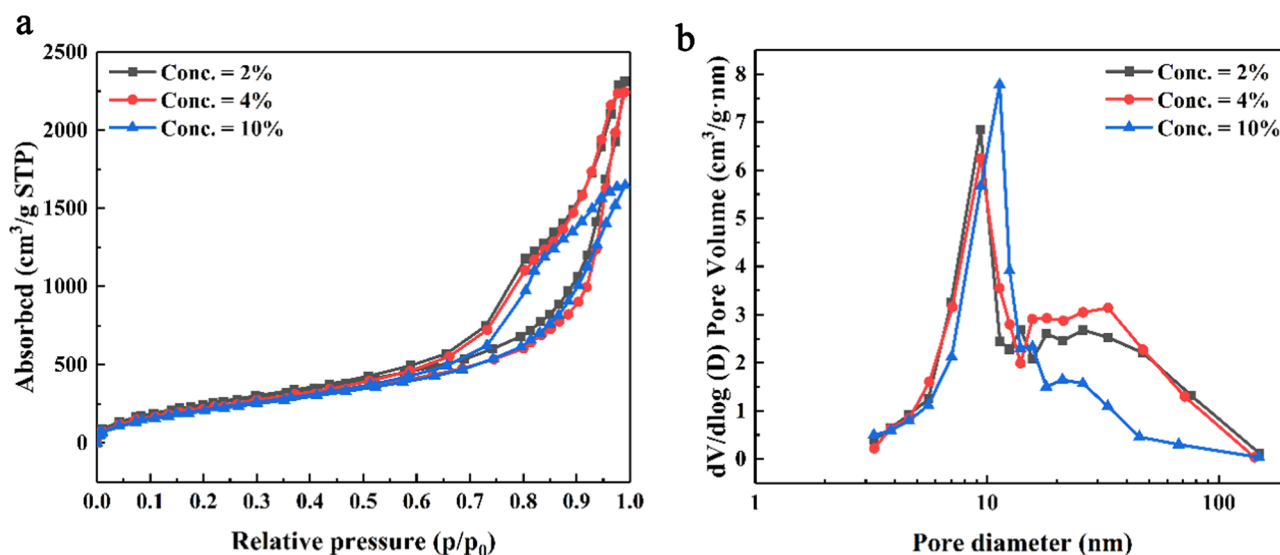


**Fig. 4** **a**  $N_2$  adsorption–desorption isotherms and **b** PSD of the DSA modified with different DMDCS concentration

**Table 2** Surface properties of DSA modified by different concentrations of DMDCS

Concentration	BET surface area ( $m^2/g$ )	Pore volume ( $cm^3/g$ )	Average pore size (nm)
2%	$990 \pm 14$	$3.6 \pm 0.3$	$11.4 \pm 0.8$
4%	$893 \pm 9$	$3.5 \pm 0.2$	$15.6 \pm 0.3$
10%	$852 \pm 8$	$3.7 \pm 0.2$	$12.0 \pm 0.4$

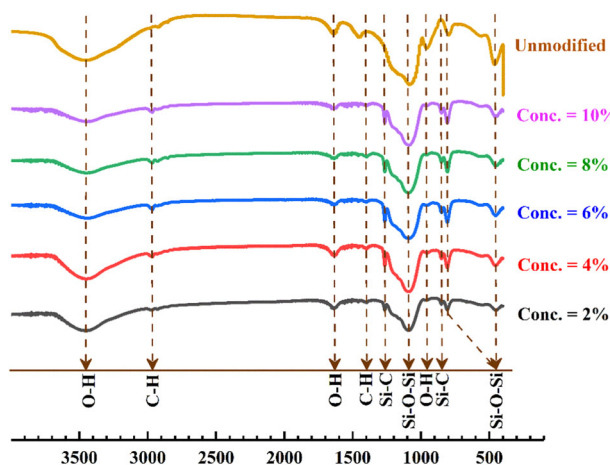


**Fig. 5** The FTIR spectra of unmodified silica xerogels and DSA modified by different concentrations of DMDCS

In term of a thermal reaction process, the onset temperatures and the temperatures corresponding to the fastest reaction rate are two important parameters to determine the thermal stability of a material, which are usually denoted as  $T_{onset}$  and  $T_{peak}$ , respectively. For hydrophobic SA, when the temperature exceeds  $T_{onset}$ , SA becomes hydrophilic

gradually, resulting in adsorption of moisture in air and further causing a continuous deterioration of physical properties.

As seen in Table 3, the  $T_{onset}$  of the DSA and TSA are 238 and 242 °C, respectively, while the  $T_{peak}$  of the DSA and TSA are 265 and 273 °C, respectively. Comparing the  $T_{onset}$  and  $T_{peak}$  between the DSA and TSA, it can draw a conclusion that they have close thermal stability. Furthermore, the weight losses from the onset temperature to the end temperature during the exothermic reaction can be approximately regarded as the  $-CH_3$  content on SA. Accordingly, the  $-CH_3$  contents of DSA and TSA are calculated as about 6 and 9% through the TG curves, respectively. This demonstrates that the DSA possesses about 33% less  $-CH_3$  groups than that of the TSA. From the perspective of the combustible component, the DSA further presents a lower thermal hazard compared with the TSA.

### 3.3 Kinetic analysis

For conversion rate  $\alpha$  within 0.1 ~ 0.9, the two methods, i.e., FWO and KAS methods, are employed to calculate the apparent activation energy  $E_a$ . The optimum fitting lines are confirmed by the least square method. Within  $\alpha = 0.1-0.9$ , the fitted lines for  $\ln(\beta) \sim 1/T$  in Fig. 8a and  $\ln(\beta/T^2) \sim 1/T$  in Fig. 8b all present high linearity. Finally, the apparent activation energies are calculated according to the slopes of the corresponding fitted lines.

The variations of the apparent activation energy are presented in Fig. 9, which indicates that the apparent activation energies calculated from the FWO method and the KAS method are almost the same. Note that the apparent

**Fig. 6** **a** The change of the water contact angle along with the DMDCS concentration and **b** the photograph of contact angle at the DMDCS concentration being 4%

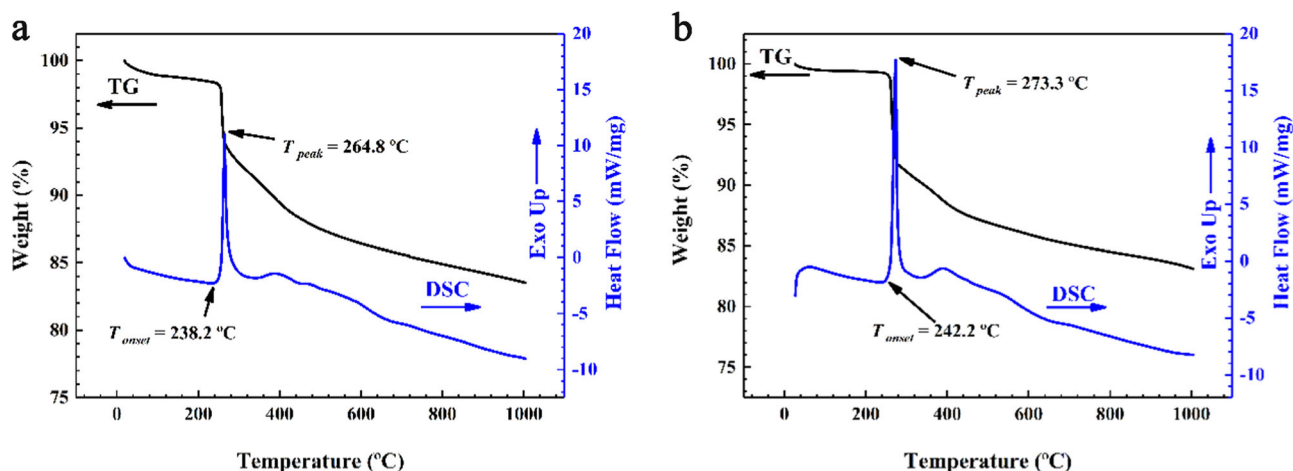
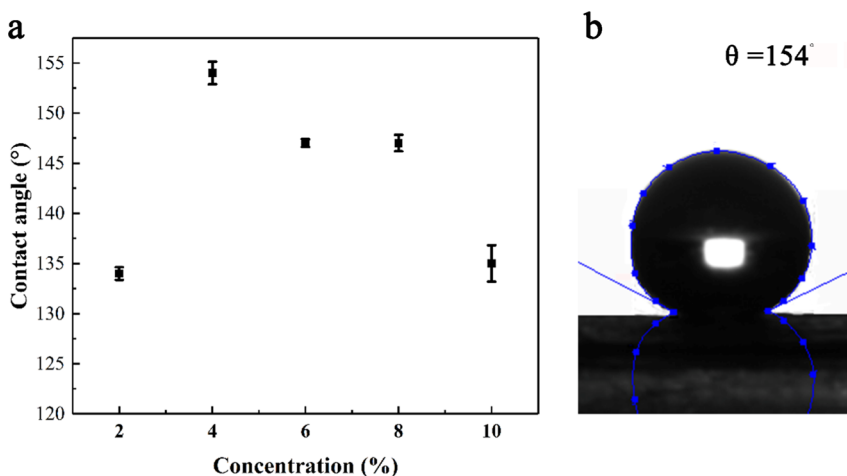


**Fig. 7** TG-DSC curves of **a** the DSA and **b** TSA under 10 °C/min in air

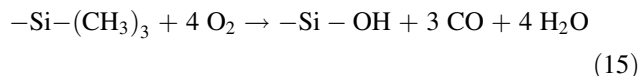
**Table 3** Corresponding  $T_{onset}$ ,  $T_{peak}$ , and  $-CH_3$  content of the DSA and TSA

Sample	$T_{onset}$ (°C)	$T_{peak}$ (°C)	$-CH_3$ content (%)
DSA	238	265	6
TSA	242	273	9

activation energies calculated within  $\alpha < 0.2$  and  $\alpha > 0.8$  are not reliable. Because the evaporation of some remained solvent in the initial stage and some residue are no longer decomposed in the final stage therefore it may cause an error in calculating kinetic parameters [39]. Without considering the initial and final stage of the thermal oxidation, namely defining  $\alpha = 0.2-0.8$ , the conspicuous two-segment process is presented and the cut-off point is set as  $\alpha = 0.5$ , which declares the thermal oxidation processes for hydrophobic DSA are multistage.

In Stage I, namely  $\alpha = 0.2-0.5$ , the change of  $E_a$  shows an obvious increasing trend with a higher  $\alpha$  and the  $E_a$  rises

rapidly to the maximum, 257.1 kJ/mol. This stage mainly corresponds to the decomposition of organic groups on skeletons. As the thermal oxidation of Si-CH<sub>3</sub> groups proceeds, more Si-OH groups are generated [11, 14], which can be expressed as Eq. (15).



Simultaneously, the condensation reaction among the produced Si-OH groups would launch and generate more water in the process subsequently. Accompanied by these reactions, the  $E_a$  increases rapidly [40] and rises to the maximum at  $\alpha = 0.5$ . In Stage II within  $\alpha = 0.5-0.8$ ,  $E_a$  decreases promptly, which indicates that certain intermediates may facilitate the decomposition and oxidation of organic groups [11]. As it is known to all, the  $E_a$  reflects an energy obstacle that must be overcome for proceeding a chemical reaction. Therefore, a higher value of  $E_a$  implies it is more difficult for a chemical reaction to occur.



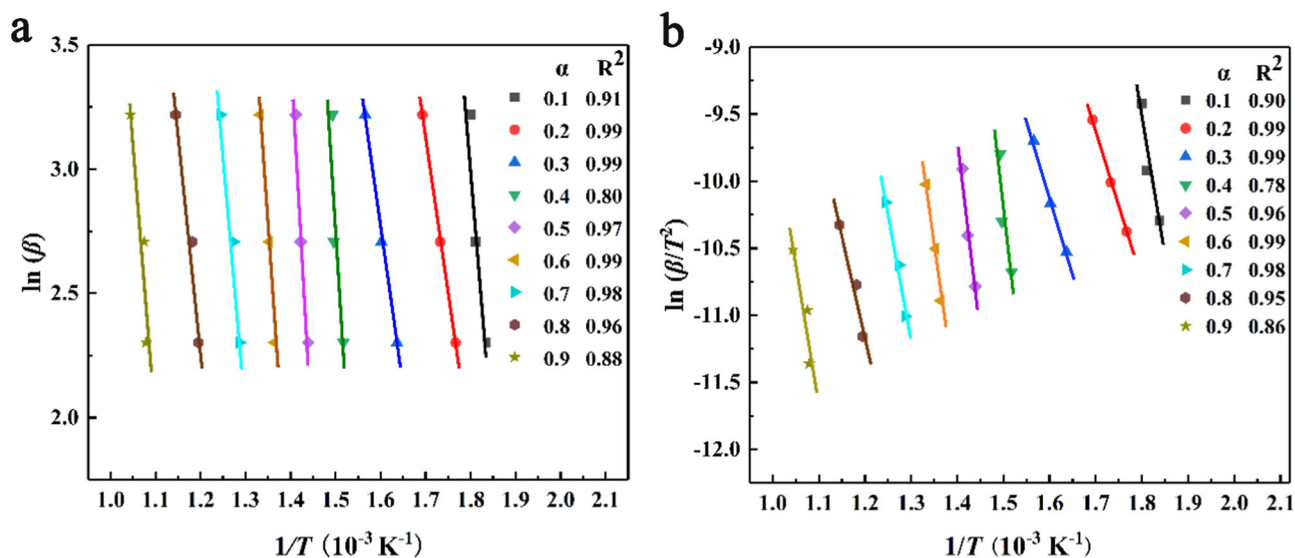


Fig. 8 Fitted lines based on **a** the OFW method and **b** the KAS method

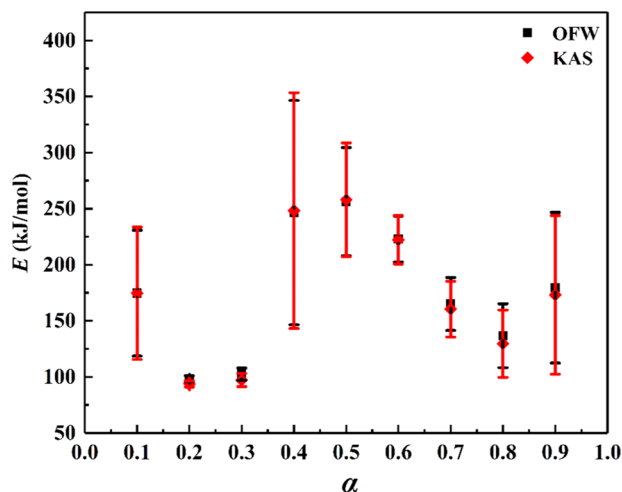


Fig. 9  $E_a$  along the increasing  $\alpha$  for the DSA

### 3.4 Thermodynamic analysis

Table 4 shows the thermodynamic parameters including pre-exponential factor ( $A$ ), the changes of enthalpy ( $\Delta H$ ), free Gibbs energy ( $\Delta G$ ), and entropy ( $\Delta S$ ), which are calculated by using the average  $E_a$  obtained from the two methods.

The values of the pre-exponential factor ( $A$ ) range from  $8.2 \times 10^6$  to  $4.2 \times 10^{22}$ , which are directly related to the material structure to some extent. Besides, it can also be used to describe the complex reactions that occur during decomposition [41]. Within  $\alpha = 0.2$ – $0.5$  for Stage I, the values of  $A$  increase rapidly indicating a higher rate of molecular collisions and an increasing need for energy during the pyrolysis of the DSA [42]. On the contrary, the

Table 4 Thermodynamic parameters of the DSA under  $10^\circ\text{C}/\text{min}$

$\alpha$	$A$ ( $\text{s}^{-1}$ )	$\Delta H$ (kJ/mol)	$\Delta G$ (kJ/mol)	$\Delta S$ (J/K/mol)
0.1	$4.2 \times 10^{14}$	170	158	22
0.2	$8.2 \times 10^6$	92	161	−126
0.3	$1.9 \times 10^7$	95	161	−119
0.4	$4.8 \times 10^{21}$	243	157	157
0.5	$4.2 \times 10^{22}$	253	156	175
0.6	$1.9 \times 10^{19}$	218	157	111
0.7	$4.0 \times 10^{13}$	158	158	0
0.8	$3.8 \times 10^{10}$	129	159	−56
0.9	$6.2 \times 10^{14}$	172	158	25

values of  $A$  decrease sharply at stage II, which just keep consistent with the change of apparent activation energy.

The change of enthalpy ( $\Delta H$ ) reflects the energy difference between the reactants and products, which nearly has the same change with the  $E_a$ . Furthermore, all the  $\Delta H$  is larger than zero indicates an exothermic reaction of the pyrolysis process. The change of Gibbs free energy ( $\Delta G$ ) means the total increase in energy of the reaction system for the reagents and the formation of the activated complex [35, 42–44]. During the pyrolysis process of the DSA, the  $\Delta G$  has no obvious changes with a slight fluctuation from 156 to 161 kJ/mol. In other words, the total energy required in the pyrolysis process has no significant difference in the whole process and the whole pyrolysis process cannot be carried out spontaneously without external energy supply. The entropy ( $\Delta S$ ) represents the disorder degree of a system, which can be expressed as a state parameter [42]. As listed in Table 4, the  $\Delta S$  ranges within −126 to 175 J/K/mol. The negative values indicate that the degree of disorder

of products is lower compared with the initial reactants due to the external energy supply [42, 43, 45], and vice versa.

### 3.5 Thermal hazard assessment

The GCV can reflect the total heat release of a material in the condition of complete combustion precisely [46–50], which usually measured using an oxygen bomb calorimeter. As illustrated in Fig. 10, the GCV of the TSA is 10.1 MJ/kg while that of DSA is 8.9 MJ/kg. Compared with the TSA, the DSA possesses about 12% reduction in GCV. Furthermore, the average apparent activation energy of the TSA and DSA is calculated as  $97 \pm 18$  and  $174 \pm 42$  kJ/mol, respectively. That is to say, the DSA are harder to activate the thermal oxidation process compared with the TSA.

Here, we further give a more comprehensive thermal hazard assessment on the DSA. From the TG–DSC analyses, the DSA nearly has the same thermal stability as the typical TSA, which has been indicated by the close  $T_{\text{onset}}$  and  $T_{\text{peak}}$ . The specific thermodynamic parameters have demonstrated that the whole pyrolysis process of the DSA cannot occur spontaneously without external energy supply. The apparent activation energy of the DSA is far larger than that of the TSA, which indicates that more energy is needed to launch the thermal oxidation reaction of the DSA. Furthermore, a more direct characterization for thermal hazard is carried out by the GCV measurement, which has clarified that the DSA possesses a lower GCV than the TSA. This result can be supported by the reduction in  $-\text{CH}_3$  content for the TSA. All of these indicate that the DSA has better fire retardancy than the TSA. In one word, it can be concluded that the DSA has a lower potential thermal hazard compared to the TSA.

## 4 Conclusions

In this study, DMDCS modified hydrophobic silica aerogels (DSA) were prepared successfully. The effects of DMDCS concentration were investigated and the optimum was confirmed as 4%. Based on the as-prepared DSA, we focused on the assessment of their thermal hazards and some conclusions were drawn as follow.

The TG–DSC analyses indicated that the DSA had similar thermal stability with the TSA but possessed less  $-\text{CH}_3$  content compared with the TSA. The cut-off point was set at  $\alpha = 0.5$ , which divided the whole thermal oxidation process into two stages, i.e.,  $\alpha = 0.2\text{--}0.5$  for Stage I and  $\alpha = 0.5\text{--}0.8$  for Stage II. Besides, the average apparent activation energy of the DSA was far larger than that of the TSA, which implied that more energy was required to launch the thermal oxidation reaction. On the aspect of thermodynamics, all the  $\Delta H$  were larger than zero during

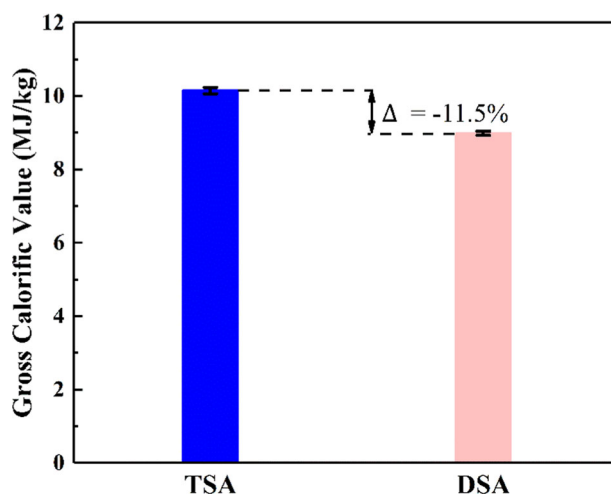


Fig. 10 GCV of the TSA and DSA

the pyrolysis, indicated the attribution of an exothermic reaction. The  $\Delta G$  fluctuating slightly within 156–161 kJ/mol demonstrated that the thermal oxidation of the DSA cannot occur spontaneously without external energy supply. Furthermore, the GCV of the DSA was reduced by about 12% compared with that of the TSA. All these kinetic and thermodynamic parameters revealed that the DSA lowered the thermal hazard to some extent, which provided a technical basis for further reducing the thermal hazards of hydrophobic SA.

**Acknowledgements** This work was supported by the National Natural Science Foundation of China (No. 51904336), the Fundamental Research Funds for the Central Universities (Nos. 202501003 and 202045001) and the China Scholarship Council (No. 201806375007). Furthermore, we really appreciate the anonymous reviewer for the constructive comments and the co-editor Florence Babonneau for the resubmission opportunity.

### Compliance with ethical standards

**Conflict of interest** The authors declare that they have no conflict of interest.

**Publisher's note** Springer Nature remains neutral with regard to jurisdictional claims in published maps and institutional affiliations.

## References

- Husing N, Schubert U (1998) Aerogels-airy materials: chemistry, structure, and properties. *Angew Chem Int Ed Engl* 37:22–45. [https://doi.org/10.1002/\(SICI\)1521-3773\(19980202\)37:1/2<22::AID-ANIE22>3.0.CO;2-I](https://doi.org/10.1002/(SICI)1521-3773(19980202)37:1/2<22::AID-ANIE22>3.0.CO;2-I)
- Cuce E, Cuce PM, Wood CJ, Riffat SB (2014) Toward aerogel based thermal superinsulation in buildings: a comprehensive review. *Renew Sustain Energy Rev* 34:273–299. <https://doi.org/10.1016/j.rser.2014.03.017>

3. Randall JP, Meador MAB, Jana SC (2011) Tailoring mechanical properties of aerogels for aerospace applications. *ACS Appl Mater Interfaces* 3:613–626. <https://doi.org/10.1021/am200007n>
4. Rao AV, Hegde ND, Hirashima H (2007) Absorption and desorption of organic liquids in elastic superhydrophobic silica aerogels. *J Colloid Interface Sci* 305:124–132. <https://doi.org/10.1016/j.jcis.2006.09.025>
5. Zhao Y, Liang Y, Zhao X et al. (2011) Preparation and microstructure of CuO-CoO-MnO/SiO<sub>2</sub> nanocomposite aerogels and xerogels as catalyst carriers. *Prog Nat Sci Mater Int* 21:330–335. [https://doi.org/10.1016/S1002-0071\(12\)60065-3](https://doi.org/10.1016/S1002-0071(12)60065-3)
6. Alnaief M, Smirnova I (2010) Effect of surface functionalization of silica aerogel on their adsorptive and release properties. *J Non-Cryst Solids* 356:1644–1649. <https://doi.org/10.1016/j.jnoncrysol.2010.06.027>
7. Koebel M, Rigacci A, Achard P (2012) Aerogel-based thermal superinsulation: an overview. *J Sol-Gel Sci Technol* 63:315–339. <https://doi.org/10.1007/s10971-012-2792-9>
8. Baetens R, Jelle BP, Gustavsen A (2011) Aerogel insulation for building applications: a state-of-the-art review. *Energy Build* 43:761–769. <https://doi.org/10.1016/j.enbuild.2010.12.012>
9. Wang B, Wu C, Kang L et al. (2018) Work safety in China's thirteenth five-year plan period (2016–2020): current status, new challenges and future tasks. *Saf Sci* 104:164–178. <https://doi.org/10.1016/j.ssci.2018.01.012>
10. Mahadik SA, Pedraza F, Parale VG, Park H-H (2016) Organically modified silica aerogel with different functional silylating agents and effect on their physico-chemical properties. *J Non-Cryst Solids* 453:164–171. <https://doi.org/10.1016/j.jnoncrysol.2016.08.035>
11. Li Z, Cheng X, Shi L et al. (2016) Flammability and oxidation kinetics of hydrophobic silica aerogels. *J Hazard Mater* 320:350–358. <https://doi.org/10.1016/j.jhazmat.2016.07.054>
12. Li Z, Huang S, Shi L et al. (2019) Reducing the flammability of hydrophobic silica aerogels by doping with hydroxides. *J Hazard Mater* 373:536–546. <https://doi.org/10.1016/j.jhazmat.2019.03.112>
13. Ghazi Wakili K, Remhof A (2017) Reaction of aerogel containing ceramic fibre insulation to fire exposure. *Fire Mater* 41:29–39. <https://doi.org/10.1002/fam.2367>
14. He S, Huang Y, Chen G et al. (2019) Effect of heat treatment on hydrophobic silica aerogel. *J Hazard Mater* 362:294–302. <https://doi.org/10.1016/j.jhazmat.2018.08.087>
15. Zhang W, Li Z, Shi L et al. (2019) Methyltrichlorosilane modified hydrophobic silica aerogels and their kinetic and thermodynamic behaviors. *J Sol-Gel Sci Technol* 89:448–457. <https://doi.org/10.1007/s10971-018-4882-9>
16. Luo Y, Li Z, Zhang W et al. (2019) Rapid synthesis and characterization of ambient pressure dried monolithic silica aerogels in ethanol/water co-solvent system. *J Non-Cryst Solids* 503:214–223. <https://doi.org/10.1016/j.jnoncrysol.2018.09.049>
17. Li Z, Cheng X, Gong L et al. (2018) Enhanced flame retardancy of hydrophobic silica aerogels by using sodium silicate as precursor and phosphoric acid as catalyst. *J Non-Cryst Solids* 481:267–275. <https://doi.org/10.1016/j.jnoncrysol.2017.10.053>
18. Malfait WJ, Zhao S, Verel R et al. (2015) Surface chemistry of hydrophobic silica aerogels. *Chem Mater* 27:6737–6745. <https://doi.org/10.1021/acs.chemmater.5b02801>
19. Malfait WJ, Jurányi F, Zhao S et al. (2017) Dynamics of silica aerogel's hydrophobic groups: a quasielastic neutron scattering study. *J Phys Chem C* 121:20335–20344. <https://doi.org/10.1021/acs.jpcc.7b06011>
20. Iswar S, Griffa M, Kaufmann R et al. (2019) Effect of aging on thermal conductivity of fiber-reinforced aerogel composites: an X-ray tomography study. *Microporous Mesoporous Mater* 278:289–296. <https://doi.org/10.1016/j.micromeso.2018.12.006>
21. Li Z, Cheng X, He S et al. (2015) Characteristics of ambient-pressure-dried aerogels synthesized via different surface modification methods. *J Sol-Gel Sci Technol* 76:138–149. <https://doi.org/10.1007/s10971-015-3760-y>
22. Soleimani Dorcheh A, Abbasi MH (2008) Silica aerogel; synthesis, properties and characterization. *J Mater Process Technol* 199:10–26. <https://doi.org/10.1016/j.jmatprotec.2007.10.060>
23. Malfait WJ, Verel R, Koebel MM (2014) Hydrophobization of silica aerogels: insights from quantitative solid-state NMR spectroscopy. *J Phys Chem C* 118:25545–25554. <https://doi.org/10.1021/jp5082643>
24. Schneider CA, Rasband WS, Eliceiri KW (2012) NIH image to imageJ: 25 years of image analysis. *Nat Methods* 9:671–675. <https://doi.org/10.1038/nmeth.2089>
25. Brunauer S, Emmett PH, Teller E (1938) Adsorption of gases in multimolecular layers. *J Am Chem Soc* 60:309–319. <https://doi.org/10.1021/ja01269a023>
26. Barrett EP, Joyner LG, Halenda PP (1951) The determination of pore volume and area distributions in porous substances. I. Computations from nitrogen isotherms. *J Am Chem Soc* 73:373–380. <https://doi.org/10.1021/ja01145a126>
27. Wu X, Fan M, Shen X et al. (2018) Silica aerogels formed from soluble silicates and methyl trimethoxysilane (MTMS) using CO<sub>2</sub> gas as a gelation agent. *Ceram Int* 44:821–829. <https://doi.org/10.1016/j.ceramint.2017.10.005>
28. Cheng X, Li C, Shi X et al. (2017) Rapid synthesis of ambient pressure dried monolithic silica aerogels using water as the only solvent. *Mater Lett* 204:157–160. <https://doi.org/10.1016/j.matlet.2017.05.107>
29. He S, Sun G, Cheng X et al. (2017) Nanoporous SiO<sub>2</sub> grafted aramid fibers with low thermal conductivity. *Compos Sci Technol* 146:91–98. <https://doi.org/10.1016/j.compscitech.2017.04.021>
30. Gurav JL, Rao AV, Rao AP et al. (2009) Physical properties of sodium silicate based silica aerogels prepared by single step sol-gel process dried at ambient pressure. *J Alloy Compd* 476:397–402. <https://doi.org/10.1016/j.jallcom.2008.09.029>
31. Jiang L, Zhang D, Li M et al. (2018) Pyrolytic behavior of waste extruded polystyrene and rigid polyurethane by multi kinetics methods and Py-GC/MS. *Fuel* 222:11–20. <https://doi.org/10.1016/j.fuel.2018.02.143>
32. Flynn JH, Wall LA (1966) A quick, direct method for the determination of activation energy from thermogravimetric data. *J Polym Sci Part C Polym Lett* 4:323–328
33. Doyle CD (2010) Estimating isothermal life from thermogravimetric data. *J Appl Polym Sci* 6:639–642. <https://doi.org/10.1002/app.1962.070062406>
34. Ozawa T (1992) Estimation of activation energy by isoconversion methods. *Thermochim Acta* 203:159–165. [https://doi.org/10.1016/0040-6031\(92\)85192-X](https://doi.org/10.1016/0040-6031(92)85192-X)
35. Domingos Maia AA, de Moraes LC (2016) Kinetic parameters of red pepper waste as biomass to solid biofuel. *Bioresour Technol* 204:157–163. <https://doi.org/10.1016/j.biortech.2015.12.055>
36. Rojas F, Kornhauser I, Felipe C et al. (2002) Capillary condensation in heterogeneous mesoporous networks consisting of variable connectivity and pore-size correlation. *Phys Chem Chem Phys* 4:2346–2355. <https://doi.org/10.1039/b108785a>
37. Gurav JL, Rao AV, Rao AP et al. (2009) Physical properties of sodium silicate based silica aerogels prepared by single step sol-gel process dried at ambient pressure. *J Alloy Compd* 476:397–402. <https://doi.org/10.1016/j.jallcom.2008.09.029>
38. Rao AP, Rao AV, Pajonk GM (2007) Hydrophobic and physical properties of the ambient pressure dried silica aerogels with sodium silicate precursor using various surface modification agents. *Appl Surf Sci* 253:6032–6040. <https://doi.org/10.1016/j.apsusc.2006.12.117>
39. Kim YS, Kim YS, Kim SH (2010) Investigation of thermodynamic parameters in the thermal decomposition of plastic

- waste-waste lube oil compounds. *Environ Sci Technol* 44:5313–5317. <https://doi.org/10.1021/es101163e>
40. Zhuravlev LT (2000) The surface chemistry of amorphous silica. Zhuravlev model. *Colloids Surf Physicochem Eng Asp* 173:1–38. [https://doi.org/10.1016/S0927-7757\(00\)00556-2](https://doi.org/10.1016/S0927-7757(00)00556-2)
41. Turmanova SC, Genieva SD, Dimitrova AS, Vlaev LT (2008) Non-isothermal degradation kinetics of filled with rice husk ash polypropylene composites. *Express Polym Lett* 2:133–146. <https://doi.org/10.3144/expresspolymlett.2008.18>
42. Yuan X, He T, Cao H, Yuan Q (2017) Cattle manure pyrolysis process: kinetic and thermodynamic analysis with isoconversional methods. *Renew Energy* 107:489–496. <https://doi.org/10.1016/j.renene.2017.02.026>
43. Xu Y, Chen B (2013) Investigation of thermodynamic parameters in the pyrolysis conversion of biomass and manure to biochars using thermogravimetric analysis. *Bioresour Technol* 146:485–493. <https://doi.org/10.1016/j.biortech.2013.07.086>
44. Sheng J, Ji D, Yu F et al. (2014) Influence of chemical treatment on rice straw pyrolysis by TG-FTIR. *Ieri Procedia* 8:30–34. <https://doi.org/10.1016/j.ieri.2014.09.006>
45. Kim YS, Kim YS, Kim SH (2010) Investigation of thermodynamic parameters in the thermal decomposition of plastic waste-waste lube oil compounds. *Environ Sci Technol* 44:5313–5317. <https://doi.org/10.1021/es101163e>
46. Mancini M, Rinnan A, Pizzi A, Toscano G (2018) Prediction of gross calorific value and ash content of woodchip samples by means of FT-NIR spectroscopy. *Fuel Process Technol* 169:77–83. <https://doi.org/10.1016/j.fuproc.2017.09.021>
47. Mesroghli Sh, Jorjani E, Chehreh Chelgani S (2009) Estimation of gross calorific value based on coal analysis using regression and artificial neural networks. *Int J Coal Geol* 79:49–54. <https://doi.org/10.1016/j.coal.2009.04.002>
48. Patel SU, Kumar BJ, Badhe YP et al. (2007) Estimation of gross calorific value of coals using artificial neural networks. *Fuel* 86:334–344. <https://doi.org/10.1016/j.fuel.2006.07.036>
49. Yamazaki I, Mimuro M, Murao T et al. (1984) Excitation energy transfer in the light harvesting antenna system of the red ALGA *Porphyridium cruentum* and the blue-green ALGA *Anacystis nidulans*: analysis of time-resolved fluorescence spectra. *Photochem Photobiol* 39:233–240. <https://doi.org/10.1111/j.1751-1097.1984.tb03432.x>
50. Feng Q, Zhang J, Zhang X, Wen S (2015) Proximate analysis based prediction of gross calorific value of coals: a comparison of support vector machine, alternating conditional expectation and artificial neural network. *Fuel Process Technol* 129:120–129. <https://doi.org/10.1016/j.fuproc.2014.09.001>